

Confronting double-detonation sub-Chandrasekhar models with the low-luminosity suppression of Type Ia supernovae

Arka Ghosh^{1*} and Doron Kushnir²

¹ *Physics Department, Ben-Gurion University of the Negev, Be'er-Sheva 84105, Israel*

² *Dept. of Particle Phys. & Astrophys., Weizmann Institute of Science, Rehovot 76100, Israel*

Accepted XXX. Received YYY; in original form ZZZ

ABSTRACT

Type Ia supernovae (SNe Ia) are likely the thermonuclear explosions of carbon-oxygen (CO) white-dwarf (WD) stars, but their progenitor systems remain elusive. Recently, Sharon & Kushnir (2022) used The Zwicky Transient Facility Bright Transient Survey to construct a synthesized ⁵⁶Ni mass, M_{Ni56} , distribution of SNe Ia. They found that the rate of low-luminosity ($M_{\text{Ni56}} \approx 0.15 M_{\odot}$) SNe Ia is lower by a factor of ~ 10 than the more common $M_{\text{Ni56}} \approx 0.7 M_{\odot}$ events. We here show that in order for the double-detonation model (DDM, in which a propagating thermonuclear detonation wave, TNDW, within a thin helium shell surrounding a sub-Chandrasekhar mass CO core triggers a TNDW within the core) to explain this low-luminosity suppression, the probability of a low-mass ($\approx 0.85 M_{\odot}$) WD explosion should be ~ 100 -fold lower than that of a high-mass ($\approx 1.05 M_{\odot}$) WD. One possible explanation is that the ignition of low-mass CO cores is somehow suppressed. We use accurate one-dimensional numerical simulations to show that if a TNDW is able to propagate within the helium shell, then the ignition within the CO core is guaranteed (resolved here for the first time in a full-star simulation), even for $0.7 M_{\odot}$ WDs, providing no natural explanation for the low-luminosity suppression. DDM could explain the low-luminosity suppression if the mass distribution of primary WDs in close binaries is dramatically different from the field distribution; if the Helium shell ignition probability is suppressed for low-mass WDs; or if multidimensional perturbations significantly change our results.

Key words: hydrodynamics – shock waves – supernovae: general

1 INTRODUCTION

Type Ia supernovae (SNe Ia) are likely the thermonuclear explosions of carbon-oxygen (CO) white-dwarf (WD) stars, but their progenitor systems remain elusive (see Maoz, Mannucci & Nelemans 2014, for a review). Recently, Sharon & Kushnir (2022) used The Zwicky Transient Facility Bright Transient Survey (ZTF BTS; Fremling et al. 2020; Perley et al. 2020) to construct the luminosity function and the synthesized ⁵⁶Ni mass, M_{Ni56} , distributions of SNe Ia. They found that the distributions are unimodal, with their peaks in agreement with previous results, but feature a much lower rate of dim and luminous events (see black line in Figure 1). We focus in this paper on the ~ 10 -fold low-luminosity ($M_{\text{Ni56}} \approx 0.15 M_{\odot}$) SNe Ia suppression rate compared to the more common $M_{\text{Ni56}} \approx 0.7 M_{\odot}$ events. This low-luminosity suppression can be used to discriminate between SNe Ia models. Specifically, we show that the prediction of the "double-detonation model" (DDM; Nomoto

1982a,b; Livne 1990; Woosley & Weaver 1994) is in apparent contradiction with the low-luminosity suppression.

The DDM has been studied extensively (Hoefflich & Khokhlov 1996; Nugent et al. 1997; Bildsten et al. 2007; Fink, Hillebrandt & Röpke 2007; Fink et al. 2010; Kromer et al. 2010; Woosley & Kasen 2011; Moore et al. 2013; Shen & Bildsten 2014; Shen & Moore 2014; Polin, Nugent & Kasen 2019; Townsley, et al. 2019; Gronow et al. 2020; Boos et al. 2021; Gronow et al. 2021a,b). In this model, a thermonuclear detonation wave (TNDW) propagates within a helium shell that surrounds a sub-Chandrasekhar mass CO core. The outer TNDW launches an imploding shock wave that accelerates as it implodes and can trigger a second ignition at the CO core. The outcome of such an explosion would be very similar to a central ignition of a Sub-Chandrasekhar mass CO WD (Sub-Chandra detonation, SCD), which has been heavily studied (Sim, et al. 2010; Moll, et al. 2014; Blondin, et al. 2017; Shen, et al. 2018; Bravo et al. 2019; Kushnir, Wygoda & Sharon

* E-mail: arka@post.bgu.ac.il

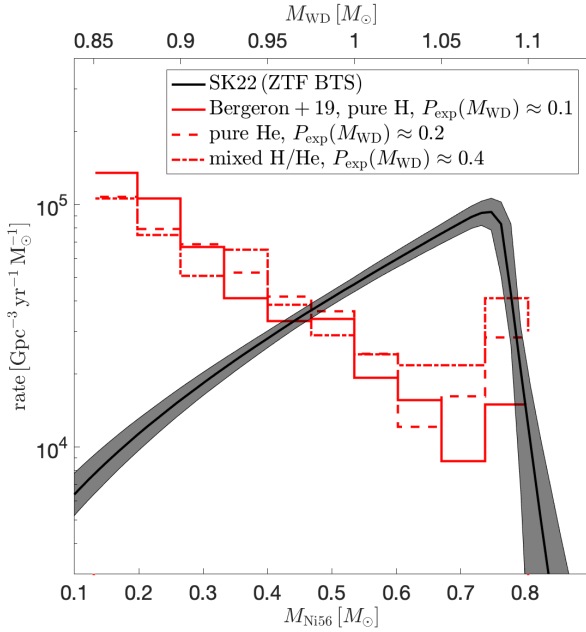


Figure 1. The $M_{\text{Ni}56}$ distribution of SNe Ia (black, Sharon & Kushnir 2022) as constructed from the ZTF BTS (Fremling et al. 2020; Perley et al. 2020). Shown are the 68-per-cent confidence level of the distribution (shaded area) and its median (black line). The rate of low-luminosity ($M_{\text{Ni}56} \approx 0.15 M_{\odot}$) SNe Ia is lower by a factor of ~ 10 compared to the more common $M_{\text{Ni}56} \approx 0.7 M_{\odot}$ events. The upper x -axis is transformed with $M_{\text{Ni}56}/M_{\odot} = 2.693(M_{\text{WD}}/M_{\odot}) - 2.165$, derived from a fit to the SCD solar-metallicity results of Kushnir, Wygoda & Sharon (2020). Red lines: The predicted $M_{\text{Ni}56}$ distribution in DDM given the mass distribution of WDs within 100 pc from the Sun (Bergeron et al. 2019), as constructed from *Gaia* data release 2 (Gaia Collaboration et al. 2018). The WDs have been fitted under the assumption of a pure hydrogen envelope (solid), a pure helium envelope (dashed), or a mixed hydrogen/helium envelope (dot-dashed). Since the relation between M_{WD} and $M_{\text{Ni}56}$ is linear for DDM in the presented range, the predicted SNe Ia rate in DDM is just the WD’s mass distribution, up to a scaling (assuming the chance that a WD explodes, P_{exp} , depends weakly on its mass in the presented range). We normalize the predicted rate with $P_{\text{exp}} \approx 0.1(0.2, 0.4)$, which leads to a similar total SNe Ia rate (since $\approx 10(5, 2.5)\%$ of WDs are within the mass range $0.85 - 1.1 M_{\odot}$ for the pure hydrogen (pure helium, mixed composition) assumption, Bergeron et al. 2019, and $\approx 1\%$ of WDs should explode to match the SNe Ia rate). Low-mass WDs ($\approx 0.85 M_{\odot}$ WDs, the progenitors of $M_{\text{Ni}56} \approx 0.15 M_{\odot}$ in the DDM) are ~ 10 -fold more common than high-mass WDs ($\approx 1.05 M_{\odot}$ WDs, the progenitors of $M_{\text{Ni}56} \approx 0.7 M_{\odot}$ in the DDM), where the ratio depends somewhat on the envelope composition assumption. In order for the DDM to agree with the low-luminosity suppression, the probability of low-mass WDs exploding should be much lower (by a factor of ~ 100) than that of high-mass WDs. Note that a very high efficiency, $P_{\text{exp}}(M_{\text{WD}} \approx 1.1 M_{\odot}) \sim 1$, of the DDM in exploding $M_{\text{WD}} \approx 1.1 M_{\odot}$ WDs is required in order to agree with the observed rate of $M_{\text{Ni}56} \approx 0.7 M_{\odot}$.

2020). The $M_{\text{Ni}56}$ is controlled by the mass of the WD, M_{WD} , where $M_{\text{Ni}56}$ monotonically increases with M_{WD} (e.g., Sim, et al. 2010; Moll, et al. 2014; Blondin, et al. 2017; Shen, et al. 2018; Bravo et al. 2019; Kushnir, Wygoda & Sharon 2020). The solar-metallicity results of Kushnir, Wygoda & Sharon (2020) can be fitted with $M_{\text{Ni}56}/M_{\odot} = 2.693(M_{\text{WD}}/M_{\odot}) - 2.165$ to better than 3 per cent accuracy in the range $0.85 \leq M_{\text{WD}}/M_{\odot} \leq 1.1$, which corresponds to the range $0.12 \lesssim M_{\text{Ni}56}/M_{\odot} \lesssim 0.8$. This

transformation is used to determine the upper x -axis of Figure 1. Since the relation between M_{WD} and $M_{\text{Ni}56}$ is linear for DDM in this range, the predicted SNe Ia rate in DDM is just the WD’s mass distribution, up to a scaling (assuming the chance that a WD explodes, P_{exp} , depends weakly on its mass in this range).

Bergeron et al. (2019) have used WDs detected by the *Gaia* mission (data release 2; Gaia Collaboration et al. 2018) to construct the mass distribution of WDs within 100 pc from the Sun. The WDs have been fitted under the assumption of a pure hydrogen envelope, a pure helium envelope, or a mixed hydrogen/helium envelope. We normalize the results of Bergeron et al. (2019, red lines in Figure 1) with $P_{\text{exp}} \approx 0.1(0.2, 0.4)$, which leads to a similar total SNe Ia rate (since $\approx 10(5, 2.5)\%$ of WDs are in the mass range $0.85 - 1.1 M_{\odot}$ for the pure hydrogen (pure helium, mixed composition) assumption, Bergeron et al. 2019, and $\approx 1\%$ of WDs should explode to match the SNe Ia rate). As can be seen in the figure, $\approx 0.85 M_{\odot}$ WDs (hereafter *low-mass WDs*, the progenitors of $M_{\text{Ni}56} \approx 0.15 M_{\odot}$ in the DDM) are more common by a factor of ~ 10 than $\approx 1.05 M_{\odot}$ WDs (hereafter *high-mass WDs*, the progenitors of $M_{\text{Ni}56} \approx 0.7 M_{\odot}$ in the DDM), where the ratio depends somewhat on the envelope composition assumption. The distribution of M_{WD} can be skewed towards higher masses in environments with an average lifetime much shorter than that of the solar environment. However this is probably irrelevant to SNe Ia, as half of all SNe Ia occur > 1 Gyr after their progenitor system forms (see, e.g., Maoz, Mannucci & Nelemans 2014, and references therein), much longer than the main-sequence lifetimes of the stars that produce a $M_{\text{WD}} = 0.85 M_{\odot}$. This is especially true for the range $0.15 \lesssim M_{\text{Ni}56}/M_{\odot} \lesssim 0.5$, which is completely dominated by old red sequence galaxies (Sharon & Kushnir 2022). Therefore, in order for the DDM to agree with the low-luminosity suppression, the probability that a low-mass WD explodes should be much lower (by a factor of ~ 100) than that of a high-mass WD. Note that a very high efficiency, $P_{\text{exp}}(M_{\text{WD}} \approx 1.1 M_{\odot}) \sim 1$, of the DDM in exploding $M_{\text{WD}} \approx 1.1 M_{\odot}$ WDs is required in order to agree with the observed rate of $M_{\text{Ni}56} \approx 0.7 M_{\odot}$.

One possibility is that the probability of a WD to be involved in a binary that leads to the required conditions for the DDM to operate is much lower for low-mass WDs than for high-mass WDs. While this probability is observationally poorly constrained and its calculation is highly uncertain, the results of binary population synthesis calculations do not support this possibility. For example, Shen, Toonen & Graur (2017) used binary population synthesis to find at merger more systems with $M_{\text{WD}} \approx 0.85 M_{\odot}$ WD than systems with $M_{\text{WD}} \approx 1.05 M_{\odot}$ WD (see their figure 2; note that systems with a non-degenerate helium star donor are not considered in this study). Nevertheless, it is difficult to rule out the possibility that the primary WDs in close binaries have a mass distribution that is significantly different from the results of Bergeron et al. (2019).

Another possibility is that the ignition probability of a TNDW within the Helium shell is suppressed for low-mass WDs. While the ignition mechanism of the Helium shell is not fully understood (see, e.g., Zingale et al. 2013; Jacobs et al. 2016; Glasner et al. 2018), one could speculate that since low-mass WDs have a lower virial temperature, then a more stringent conditions are required from the progenitor binary to achieve ignition. Alternatively, high enough density for a propagating TNDW requires more massive He shells for low-mass WDS, which can also preclude some binaries.

In this paper, we study in detail the possibility that the ignition of low-mass CO cores is somehow suppressed. Kushnir, Livne & Waxman (2012) studied the connection between the converging flows and the generation of much smaller scale

hot spots that may trigger a detonation wave, both for terrestrial applications and for the conditions at a typical (density of $\rho \sim 10^7 \text{ g cm}^{-3}$) CO core. They estimated, without presenting detailed calculations, that the critical strength of the shock (measured by R_9 , the radius in which the shock velocity is 10^9 cm s^{-1}) required for the ignition of a CO core is $R_9 \sim 0.01 \text{ km}$. The implication of this number is that any imploding shock that can accelerate to $\approx 10^9 \text{ cm s}^{-1}$ at a radius that is $\gtrsim 0.01 \text{ km}$ will ignite a TNDW in the CO core. Later on, [Shen & Bildsten \(2014\)](#) verified the value $R_9 \sim 0.01 \text{ km}$ by using detailed numerical calculations and also studied the ignition condition for a wide range of core densities. They found that the critical R_9 increases with lower core densities, which may indicate that the ignition of low-mass CO cores is suppressed. We use a one-dimensional (1D) approach in Section 3 to show that the work delivered by a piston, W_p , which mimics a TNDW in the helium shell, produces an R_9 that is many orders of magnitude larger than the critical R_9 for ignition, even for very low-mass, $M_{\text{WD}} = 0.7 - 0.85 M_{\odot}$, WDs. The large R_9 in these cases allows us to verify the ignition, by numerically resolving it in a full-star simulation for the first time (see discussion of previous attempts in Section 5). We find an upper limit of $10^{-3} M_{\odot} \text{ MeV } m_p^{-1}$ to the minimal W_p required for ignition, whereas the minimal helium shell that allows a propagating TNDW within it would deliver $\sim 10^{-2} M_{\odot} \text{ MeV } m_p^{-1}$ ([Shen & Moore 2014](#)). The fact that the upper limit we provide for W_p is much smaller than what could be reasonably delivered shows that the ignition is robust.

In Section 2, we describe the 1D setup we implemented using the hydrodynamical code VULCAN (Lagrangian, hereafter VID; for details, see [Livne 1993](#)), which includes a new accurate and efficient burning scheme ([Kushnir & Katz 2020](#)). In Section 3, we show that $W_p = 10^{-3} M_{\odot} \text{ MeV } m_p^{-1}$ is sufficient to ignite TNDW, even for very low-mass, $M_{\text{WD}} = 0.7 - 0.85 M_{\odot}$, WDs. In Section 4, we provide a 1D example of a successful core ignition with $W_p = 10^{-3} M_{\odot} \text{ MeV } m_p^{-1}$. The purpose of this example is to clarify the ignition process behind accelerating shock ([Kushnir, Livne & Waxman 2012](#); [Kushnir et al. 2013](#)) and to demonstrate that our numerical scheme is able to resolve this ignition. We summarise our results in Section 5, where we also discuss the expected multi-D modification to our 1D approach. We conclude that the DDM provides no natural explanation for the low-luminosity suppression of SNe Ia.

In what follows, we normalize temperatures, $T_9 = T [\text{K}] / 10^9$, and densities, $\rho_7 = \rho [\text{g cm}^{-3}] / 10^7$. Some aspects of this work were calculated with a modified version of the MESA code¹ ([Paxton et al. 2011, 2013, 2015](#)).

2 NUMERICAL SCHEME AND SETUP

In this section, we describe the 1D setup we implemented. We describe our initial setup in Section 2.1 and the Lagrangian numerical scheme VID in Section 2.2.

2.1 Initial setup

The WD profiles are constructed using a modified version of a routine by Frank Timmes² that includes the input physics of Appendix A. The WDs are isothermal with an initial temperature

of $T_{\text{WD},9} = 0.01$. The initial composition is uniform throughout the WD, with mass fractions $X(^{12}\text{C}) = X(^{16}\text{O}) = 0.4925$ and $X(^{22}\text{Ne}) = 0.015$ (which corresponds to solar metallicity; [Kushnir, Wygoda & Sharon 2020](#)). The helium shell is not part of the model.

We approximate the work delivered by the propagating TNDW within the helium shell as a 1D piston. As we explain in Section 3, our results do not depend on the exact implementation of the piston. We therefore choose a simple parametrisation for the piston velocity, which mimics the (azimuthally averaged) velocity of the interface between the helium shell and the CO core. Unless stated otherwise, the piston's initial position, r_p , is where the initial density is $\rho_{p,7} = 0.01$, which is a typical density at the base of the helium shell. Placing r_p at a lower density significantly decreases the time step and has a minimal effect on our results; see Section 3. The velocity profile is $v = -v_p(1 - t/t_p)$ for $t \leq t_p$ (and zero otherwise), with v_p and t_p free parameters. We scan a large range of $v_p \in [1, 10] \times 10^3 \text{ km s}^{-1}$ and we find that our results are independent of the exact chosen values.

2.2 The numerical scheme

We use our modified VID version ([Kushnir & Katz 2020](#)) that is compatible with the input physics of Appendix A. Our isotope list is the 69-isotope list calibrated by [Kushnir, Wygoda & Sharon \(2020\)](#), which allows the calculation of $M_{\text{Ni}56}$ with an accuracy greater than one percent. We safely ignore weak reactions and thermal neutrino emissions ([Kushnir, Wygoda & Sharon 2020](#)). We do not use linear artificial viscosity, the Courant time-step factor is 0.25, and the maximum relative change of the density in each cell during a time-step is set to 0.01.

We use our recently developed, accurate and efficient burning scheme that allows the structure of TNDW to be resolved ([Kushnir & Katz 2020](#)). The numerical scheme contains a burning limiter that broadens the width of the TNDW while accurately preserving its internal structure. The burning limiter limits the changes in both energy and composition to a fraction f during cell sound crossing time (for faster changes, all rates are normalized by a constant factor to limit the changes). Burning is calculated in-situ by employing the required large-networks without the use of post-processing or pre-describing the conditions behind the TNDW. The scheme was tested against accurate solutions of the structure of TNDW with resolutions that are typical for multidimensional (multi-D) full-star simulations, yielding an accuracy that is better than one percent for the resolved scales (where the burning limiter is not applied) and a few percent for unresolved scales (broadened by the burning limiter). Burning is not allowed on shocks (identified as cells where $q_v/p > 0.1$, where q_v is the artificial viscosity and p is the pressure). The allowed error tolerance for the burning integration is $\delta_B = 10^{-8}$ (see [Kushnir & Katz 2020](#), for details), and we use $f = 0.1$ for the burning limiter.

The mesh includes only the WD, with the outer numerical node at r_p . The inner boundary condition is of a solid wall and the outer boundary velocity is the assumed piston velocity. All cells are initially of an equal size, Δx_0 , and the density in each cell is determined by interpolation from the original WD profile to the center of the cell.

Since the initial profile is interpolated to the mesh, it is not in strict hydrostatic equilibrium. We therefore only activate cells that are just in front of the leading shock. This is done by finding the innermost active cell with $q_v/p > 10^{-3}$, and then activating its inner node. Initially, all cells within $[r_p - 5\Delta x_0, r_p]$ are activated. The

¹ Version r7624; <https://sourceforge.net/projects/mesa/files/releases/>

² <http://cococubed.asu.edu/>

simulations are stopped 0.25 s after the imploding shock focuses to the center. This is after the outgoing shock (or a TNDW in the case of core ignition) had travelled a significant fraction of the WD radius, but before reaching the outer node.

3 THE WORK DELIVERED BY THE HELIUM SHELL

We first perform calculations without nuclear burning for $M_{\text{WD}} = 0.7, 0.8, 0.85 M_{\odot}$ and $v_p = 1, 3, 10 \times 10^3 \text{ km s}^{-1}$. For each combination of M_{WD} and v_p , we choose a few values of t_p whose corresponding W_p values bracket $10^{-3} M_{\odot} \text{ MeV } m_p^{-1}$, and we determine R_9 in each case. Since direct differencing of the shock position is too noisy to allow the determination of the shock velocity, we instead fit the shock position to a power law, $R_s = A(t - t_0)^\alpha$, which is the exact self-similar solution for an ideal gas and roughly holds in our case (with $\alpha \approx 0.75$). We determine R_9 from the fit parameters. The fit is performed over times where R_s is in the range $[10, 100] \Delta x_0$. We increase the resolution in each case, typically up to $\Delta x_0 \lesssim 1 \text{ km}$, until R_9 converges to a few percent (and R_9 is within the range of the fit). The converged values of R_9 are presented in Figure 2. As can be seen in the figure, for $W_p = 10^{-3} M_{\odot} \text{ MeV } m_p^{-1}$, we get $R_9 \sim 10\text{--}20 \text{ km}$, with a weak dependence on the value of v_p . The obtained R_9 are larger by orders of magnitude than the critical R_9 for ignition ($\sim 0.01 \text{ km}$). This result by itself is already sufficient to show that ignition in these cases is robust³. Nevertheless, we want to verify that ignition is indeed obtained. As we show in Section 4, the size of the hot spot is $\sim R_9/30$, which allows us to resolve the hot spot with modest resolution. A higher resolution would be required for lower values of W_p , but since $W_p = 10^{-3} M_{\odot} \text{ MeV } m_p^{-1}$ is already well below the minimal work that is delivered by a TNDW that propagates within the helium shell ($\sim 10^{-2} M_{\odot} \text{ MeV } m_p^{-1}$ Shen & Moore 2014), there is no need to demonstrate ignition for lower values of W_p . Simulations for $M_{\text{WD}} = 0.8 M_{\odot}$, $v_p = 3 \times 10^3 \text{ km s}^{-1}$ and $\rho_{p,7} = 10^{-3}$ (green triangles in the figure) produced only slightly modified results.

The reason that the shock dynamics mostly depends on W_p and not on the exact details of the piston stems from the dynamics of imploding shocks. As the shock accelerates, a sonic point forms behind the shock that separates the shock from the boundary. The flow between the shock and the sonic point approaches a self-similar flow (Guderley 1942), which is independent of the boundary conditions. Therefore, the piston can only affect the shock before the sonic point forms, and the flow between the shock and the sonic point mostly depends on the work delivered to the plasma prior to this time, as we demonstrated above.

We next verify directly that indeed $W_p = 10^{-3} M_{\odot} \text{ MeV } m_p^{-1}$ is sufficient for core ignition. We calculate the core ignition with nuclear burning for each combination of M_{WD} and v_p , with t_p chosen so as to deliver exactly $W_p = 10^{-3} M_{\odot} \text{ MeV } m_p^{-1}$ (9 combinations and one more with $\rho_{p,7} = 10^{-3}$ from above, see Table 1). In all cases, ignition is obtained once a high-enough resolution is employed, typically $\Delta x_0 \lesssim 1 \text{ km}$, and the hot spot is resolved (see example in Section 4). Following ignition, two TNDWs are formed, one that propagates inwards and one that propagates outwards, following which the star explodes. We, therefore, prove that

³ We verified that this is the case also for $M_{\text{WD}} = 0.5 M_{\odot}$, the lowest mass CO WDs, with $R_9 \gtrsim 10 \text{ km}$.

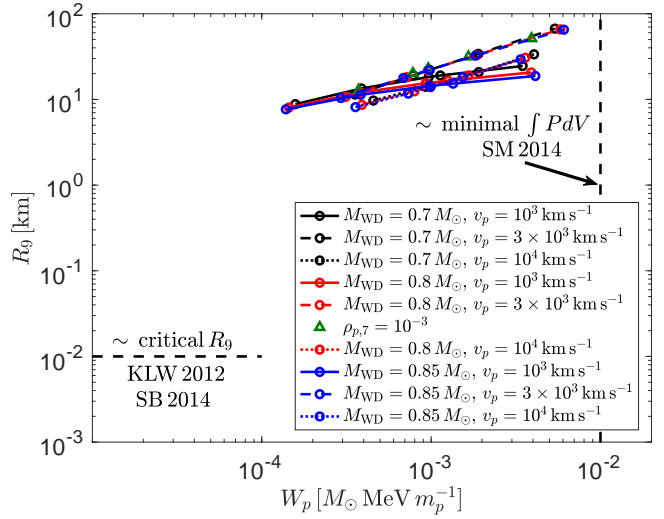


Figure 2. The converged values of R_9 (the radius in which the shock velocity is 10^9 cm s^{-1}) as a function of the work delivered by the piston, W_p . We present results for $M_{\text{WD}} = 0.7, 0.8, 0.85 M_{\odot}$ (black, red and blue, respectively) and $v_p = 1, 3, 10 \times 10^3 \text{ km s}^{-1}$ (solid, dashed and dotted, respectively). For each combination of M_{WD} and v_p , we choose a few values of t_p whose W_p values bracket $10^{-3} M_{\odot} \text{ MeV } m_p^{-1}$. For $W_p = 10^{-3} M_{\odot} \text{ MeV } m_p^{-1}$, we get $R_9 \sim 10\text{--}20 \text{ km}$, with a weak dependence on the value of v_p . The obtained R_9 are larger by orders of magnitude than the critical R_9 for ignition ($\sim 0.01 \text{ km}$; Kushnir, Livne & Waxman 2012; Shen & Bildsten 2014). This result by itself is already sufficient to show that ignition in these cases is robust. A $W_p = 10^{-3} M_{\odot} \text{ MeV } m_p^{-1}$ is well below the minimal work that can be delivered by a TNDW that propagates within the helium shell ($\sim 10^{-2} M_{\odot} \text{ MeV } m_p^{-1}$ Shen & Moore 2014). Simulations with $M_{\text{WD}} = 0.8 M_{\odot}$, $v_p = 3 \times 10^3 \text{ km s}^{-1}$ and $\rho_{p,7} = 10^{-3}$ (green triangles) show that the value of ρ_p has but a small effect on our results.

$W_p = 10^{-3} M_{\odot} \text{ MeV } m_p^{-1}$ is sufficient to ignite TNDW for all considered cases.

4 AN EXAMPLE OF A RESOLVED IGNITION

In this section, we provide an example of a successful core ignition with $M_{\text{WD}} = 0.8 M_{\odot}$, $v_p = 3 \times 10^3 \text{ km s}^{-1}$ and $t_p = 0.25 \text{ s}$ (leading to $W_p \approx 10^{-3} M_{\odot} \text{ MeV } m_p^{-1}$). In this case, we find $R_9 \approx 20 \text{ km}$ by calculating without nuclear burning. The required resolution for resolving the hot spot in a calculation that includes nuclear burning is determined by the size of the hot spot, Δr . We first provide a general analysis of the size of the hot spot, and then we present the numerical results from the example calculation.

Consider the shock wave as it approaches R_9 . We can assign for each mass coordinate, m , an explosion time, $t_{\text{exp}}(m)$, which corresponds to the time in which burning becomes very fast (we set $t = 0$ as the time in which the shock reaches the center). We can therefore write

$$t_{\text{exp}}(m) = t_{\text{sh}}(m) + t_{\epsilon} [T_{\text{sh}}(t_{\text{sh}}(m))], \quad (1)$$

where $t_{\text{sh}}(m)$ is the time in which the shock reaches the mass element (and it is negative with our choice of $t = 0$) and t_{ϵ} is the induction time, which depends on the post-shock temperature, T_{sh} . Since the induction time decreases with increasing T_{sh} , which is higher as the shock accelerates, the function $t_{\text{exp}}(m)$ has a minimum at some distance behind the shock. The induction time at this

Table 1. The configurations calculated with nuclear burning. The calibrated t_p values to deliver exactly $W_p = 10^{-3} M_\odot \text{ MeV } m_p^{-1}$ are given in the 4th column, as a function of M_{WD} (1st column), $\rho_{p,7}$ (2nd column) and v_p (3rd column).

$M_{\text{WD}} [M_\odot]$	$\rho_{p,7}$	$v_p [10^3 \text{ km s}^{-1}]$	$t_p [\text{s}]$
0.7	0.01	1	1.82
0.7	0.01	3	0.24
0.7	0.01	10	0.0107
0.8	0.01	1	1.7
0.8	0.01	3	0.25
0.8	10^{-3}	3	0.55
0.8	0.01	10	0.0123
0.85	0.01	1	1.7
0.85	0.01	3	0.26
0.85	0.01	10	0.0133

position can be found by a direct differentiation of Equation (1):

$$0 = \frac{dt_{\text{exp}}}{dt_{\text{sh}}} = 1 + \frac{dt_\varepsilon}{dT_{\text{sh}}} \frac{dT_{\text{sh}}}{dt_{\text{sh}}} = 1 - \nu\beta \frac{t_\varepsilon}{t_{\text{sh}}}, \quad (2)$$

where we assume $t_\varepsilon \propto T_{\text{sh}}^{-\nu}$ and we define

$$\frac{dT_{\text{sh}}}{dt_{\text{sh}}} = \beta \frac{T_{\text{sh}}}{t_{\text{sh}}}. \quad (3)$$

From the cross-section of $^{12}\text{C}+^{12}\text{C}$, we find for $T_{\text{sh},9} \approx 2-4$ that $\nu \approx 20-15$. We can estimate β from the self-similar solution for the shock radius

$$R_{\text{sh}} \propto t_{\text{sh}}^\alpha \Rightarrow T_{\text{sh}} \propto \dot{R}_{\text{sh}}^2 \propto t_{\text{sh}}^{2(\alpha-1)} \Rightarrow \beta = 2(\alpha-1). \quad (4)$$

We found in Section 3 for all cases $\alpha \approx 0.75$, such that $\beta \approx -0.5$, and from Equation (2), we get

$$t_\varepsilon = \frac{t_{\text{sh}}}{\nu\beta} \approx -\frac{t_{\text{sh}}}{10}. \quad (5)$$

For a successful ignition, the energy release time scale, $\varepsilon/\dot{q} \sim t_\varepsilon$, where \dot{q} is the energy injection from burning and ε is the thermal energy, needs to be shorter than the sound-crossing time of the hot spot, $\Delta r/c_s$, where c_s is the speed of sound (Zel'dovich 1980; Kushnir & Katz 2015). Therefore, the size of the hot spot during ignition satisfies $\Delta r \approx c_s t_\varepsilon \approx -c_s t_{\text{sh}}/10 \approx R_{\text{sh}}/30$, where we use $c_s \approx -0.4\dot{R}_{\text{sh}} \approx 0.4\alpha R_{\text{sh}}/t_{\text{sh}}^4$.

We demonstrate the ability to resolve the ignition region in Figure 3. The burning rate \dot{q}/ε is shown in the vicinity of the ignition location, at two snapshots separated by about 0.1 ms around the onset of ignition. The burning runaway is obtained at $R_{\text{sh}} \approx 50$ km (with $\dot{R}_{\text{sh}} \approx 7.5 \times 10^3 \text{ km s}^{-1}$), which is larger by a factor of ≈ 2.5 from the rough estimate of R_9 . Using our estimate from above, we expect a hot spot size of $\Delta r \approx 1.5$ km. As can be seen in the figure, by the time of the second snapshot, a region with such a width indeed forms, and our level of resolution is sufficient to resolve it. The speed of sound in this region is $c_s \approx 4.5 \times 10^3 \text{ km s}^{-1}$ (which roughly agrees with our estimate from above) with a sound-crossing time of ≈ 0.3 ms. The hot spot is producing energy at a rate above 100 s^{-1} , which more than doubles within 0.1 ms. A significant amount of energy is released within ~ 0.1 ms and the sound waves do not have sufficient time to distribute the excess pressure, resulting in the formation of two detonation fronts a short time later (not shown here).

⁴ For an ideal gas, the exact expression is $c_s = -\sqrt{2\gamma(\gamma-1)/(\gamma+1)^2} \dot{R}_{\text{sh}}$, where γ is the adiabatic index of the gas. We use $\gamma = 4/3$ for our estimate (that corresponds to $\alpha \approx 0.73$, see, e.g., Kushnir, Livne & Waxman 2012).

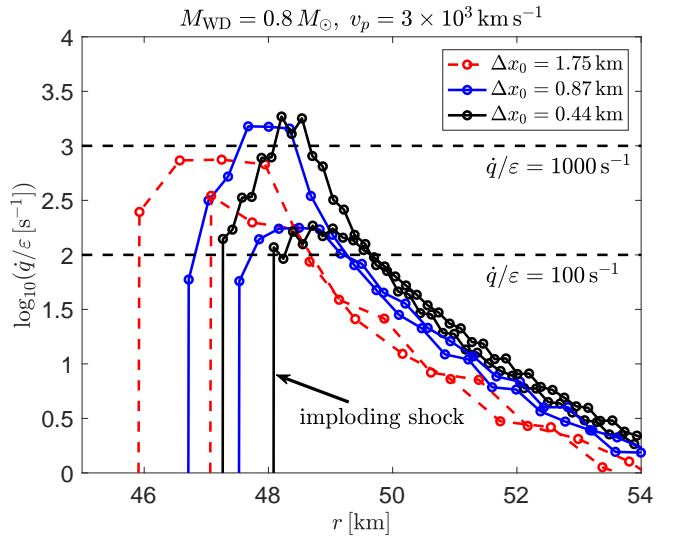


Figure 3. A resolved ignition in the $M_{\text{WD}} = 0.8 M_\odot$, $v_p = 3 \times 10^3 \text{ km s}^{-1}$ and $t_p = 0.25 \text{ s}$ (leading to $W_p \approx 10^{-3} M_\odot \text{ MeV } m_p^{-1}$) case. Snapshots of the relative burning rate, \dot{q}/ε , are presented in a series of simulations with increasing resolutions ($\Delta x_0 = 1.75, 0.87, 0.44$ km in red, blue and black, respectively), at two times separated by about 0.1 ms around the time of ignition. Note that the plasma at the ignition location is compressed by a factor of ~ 3 relative to the initial density.

5 SUMMARY AND DISCUSSION

We used 1D numerical simulations (described in Section 2) to show that if a TNDW is able to propagate within the helium shell, then ignition within the CO core is guaranteed (Section 3). We demonstrated this for $M_{\text{WD}} = 0.7, 0.8, 0.85 M_\odot$, where we were able to numerically resolve the ignition in a full-star simulation for the first time. Previous calculations of the DDM (see, e.g., Polin, Nugent & Kasen 2019; Townsley, et al. 2019; Boos et al. 2021, for recent studies) used an unstable burning scheme (or implemented a stabilizing burning limiter, but relaxed it during ignition phases), in which the ignition is presumably a result of numerical instability. For example, a "scissors mechanism" was claimed for the CO core, opposite to helium detonation ignition spot (Gronow et al. 2020, 2021a,b). In these simulations, the ignition was obtained in a density of $\rho_7 \approx 0.3$ and a temperature of $T_9 \approx 2.4$, where the burning time is $\approx 4 \times 10^{-5} \text{ s}$ (for the relevant composition of 90% ^4He , 5% ^{12}C , and 5% ^{16}O by mass),

which is much shorter than the sound-crossing time of the numerical cells, $\approx 4 \times 10^{-3}$ s (for the implemented 20 km resolution). Ignition under these conditions is obtained in the regime of numerical instability (Kushnir et al. 2013).

Our findings do not support the possibility that in the DDM the ignition of low-mass CO cores is suppressed and that the probability of low-mass WDs to explode is much lower than the probability of high-mass WDs to explode. This is in apparent contradiction with the observations that, on the one hand, the rate of low-luminosity ($M_{\text{Ni56}} \approx 0.15 M_{\odot}$) SNe Ia is suppressed by a factor of ~ 10 compared to the more common $M_{\text{Ni56}} \approx 0.7 M_{\odot}$ events (Sharon & Kushnir 2022), and that, on the other hand, $\approx 0.85 M_{\odot}$ WDs (the progenitors of $M_{\text{Ni56}} \approx 0.15 M_{\odot}$ in the DDM) are much more common (by a factor of ~ 10) than $\approx 1.05 M_{\odot}$ WDs (the progenitors of $M_{\text{Ni56}} \approx 0.7 M_{\odot}$ in the DDM) (Bergeron et al. 2019); see Figure 1. Our results indicate, therefore, that the DDM provides no natural explanation for the low-luminosity suppression of SNe Ia.

One caveat to the arguments presented here is that perhaps the probability of a WD to be involved in a binary that leads to the required conditions for the DDM to operate is much lower for low-mass WDs than for high-mass WDs (see Section 1). Additional observational and theoretical work is required to measure the mass distribution of the primary WDs in close binaries. It is also possible that the ignition probability of a TNDW within the Helium shell is suppressed for low-mass WDs (see Section 1). A study of this possibility is outside the scope of this work.

Another caveat is that we used a 1D approximation to describe the work delivered by the helium shell to the CO core. This approximation cannot take into account the multi-D structure of the imploding shock. For example, the finite travel time of the TNDW in the helium shell around the WD should have a stronger effect on lower-mass WDs due to their larger radii, which may result a larger asphericity of the imploding shock and a weakening of its strength. This effect may also lead to a shift of the focal point to lower densities away from the center of the WD. While the effect of this perturbation does not seem to be large (see, e.g., Townsley, et al. 2019; Boos et al. 2021) and the obtained R_9 is orders of magnitude greater than the critical R_9 (even at the low densities of $M_{\text{WD}} = 0.5 M_{\odot}$, see Section 3) multi-D simulations are required to verify the robustness of the ignition. Nevertheless, since WDs in the mass range of $M_{\text{WD}} = 0.85 - 1.05 M_{\odot}$ have a similar structure, we do not expect a strong dependence of the ignition properties on the WD mass in this range.

The DDM's inability to explain the low-luminosity suppression joins other challenges this model faces. Recently, Kushnir, Wygoda & Sharon (2020) used the observed $t_0 - M_{\text{Ni56}}$ relation (Sharon & Kushnir 2020a), where t_0 is the γ -rays escape time from the ejecta (measured to a few percent accuracy), to reveal a clear tension between the predictions of SCD and the observed positive correlation between t_0 and M_{Ni56} . SCD predicts an anti-correlation between t_0 and M_{Ni56} , with $t_0 \approx 30$ day for luminous ($M_{\text{Ni56}} \gtrsim 0.5 M_{\odot}$) SNe Ia, while the observed t_0 is in the range of 35 – 45 day. They showed that various uncertainties related to the physical processes and to the initial profiles of the WD are unlikely to resolve the tension with observations, although they can deteriorate the agreement with observations of low-luminosity SNe Ia. While there are some reasonable initial compositions and reaction rate values for which DDM successfully explains the low-luminosity part of the $t_0 - M_{\text{Ni56}}$ relation, this model may be in conflict with the observed ^{56}Ni mass-weighted line-of-sight velocity distribution for a large fraction of these events, as measured

from nebular spectra (Dong et al. 2015, 2018; Vallely, et al. 2020). Specifically, the ^{56}Ni velocity distribution is either double-peaked or highly shifted, which so far has not been predicted by the DDM.

The low-luminosity suppression poses a challenge for any model. As far as we know, such a suppression is not predicted by Chandrasekhar-mass models, and anyway, they are unable to explain the $t_0 - M_{\text{Ni56}}$ relation for low-luminosity SNe Ia (Wygoda et al. 2019; Sharon & Kushnir 2020b). Perhaps the direct-collision model (Kushnir et al. 2013) can explain this type of suppression, if the ignition depends strongly on the impact parameter of the colliding WDs. Such a phenomena can only be studied with 3D simulations.

6 DATA AVAILABILITY

The data underlying this article will be shared following a reasonable request to the corresponding author.

ACKNOWLEDGEMENTS

We thank Boaz Katz for suggesting the topic of this paper and for contributing to the analytical derivation of the hot spot size. We thank Subo Dong for useful discussions. DK is supported by the Israel Atomic Energy Commission – The Council for Higher Education – Pazi Foundation – a research grant from The Abramson Family Center for Young Scientists – and an ISF grant.

REFERENCES

- Bergeron P., Dufour P., Fontaine G., Coutu S., Blouin S., Genest-Beaulieu C., Bédard A., et al., 2019, *ApJ*, 876, 67. doi:10.3847/1538-4357/ab153a
- Bildsten, L., Shen, K. J., Weinberg, N. N., & Nelemans, G. 2007, *ApJ*, 662, L95
- Blondin S., Dessart L., Hillier D. J., Khokhlov A. M., 2017, *MNRAS*, 470, 157
- Boos S. J., Townsley D. M., Shen K. J., Caldwell S., Miles B. J., 2021, *ApJ*, 919, 126. doi:10.3847/1538-4357/ac07a2
- Bravo, E., Badenes, C., & Martínez-Rodríguez, H. 2019, *MNRAS*, 482, 4346
- Caughlan, G. R., & Fowler, W. A. 1988, *Atomic Data and Nuclear Data Tables*, 40, 283
- Chabrier, G., & Potekhin, A. Y. 1998, *Phys. Rev. E*, 58, 4941
- Cybert, R. H., Amthor, A. M., Ferguson, R., et al. 2010, *ApJS*, 189, 240
- Dewitt, H. E., Graboske, H. C., & Cooper, M. S. 1973, *ApJ*, 181, 439
- Dong, S., Katz, B., Kushnir, D., & Prieto, J. L. 2015, *MNRAS*, 454, L61
- Dong, S., Katz, B., Kollmeier, J. A., et al. 2018, *MNRAS*, 479, L70
- Fink M., Hillebrandt W., Röpke F. K., 2007, *A&A*, 476, 1133
- Fink, M., Röpke, F. K., Hillebrandt, W., et al. 2010, *A&A*, 514, A53
- Fremling C., Miller A. A., Sharma Y., Dugas A., Perley D. A., Taggart K., Sollerman J., et al., 2020, *ApJ*, 895, 32. doi:10.3847/1538-4357/ab8943
- Gaia Collaboration, Babusiaux C., van Leeuwen F., Barstow M. A., Jordi C., Vallenari A., Bossini D., et al., 2018, *A&A*, 616, A10. doi:10.1051/0004-6361/201832843
- Glasner S. A., Livne E., Steinberg E., Yalinewich A., Truran J. W., 2018, *MNRAS*, 476, 2238. doi:10.1093/mnras/sty421
- Gronow S., Collins C., Ohlmann S. T., Pakmor R., Kromer M., Seitzzahl I. R., Sim S. A., et al., 2020, *A&A*, 635, A169. doi:10.1051/0004-6361/201936494
- Gronow S., Côté B., Lach F., Seitzzahl I. R., Collins C. E., Sim S. A., Röpke F. K., 2021, *A&A*, 656, A94. doi:10.1051/0004-6361/202140881

Gronow S., Collins C. E., Sim S. A., Röpke F. K., 2021b, *A&A*, 649, A155. doi:10.1051/0004-6361/202039954

Guderley, G. 1942, *Luftfahrtforschung*, 19, 302

Hansen, J. P., Torrie, G. M., & Vieillefosse, P. 1977, *Phys. Rev. A*, 16, 2153

Hoefflich, P., & Khokhlov, A. 1996, *ApJ*, 457, 500

Jacobs A. M., Zingale M., Nonaka A., Almgren A. S., Bell J. B., 2016, *ApJ*, 827, 84. doi:10.3847/0004-637X/827/1/84

Khokhlov, A. M. 1988, *Ap&SS*, 149, 91

Kromer, M., Sim, S. A., Fink, M., et al. 2010, *ApJ*, 719, 1067

Kushnir D., Livne E., Waxman E., 2012, *ApJ*, 752, 89

Kushnir, D., Katz, B., Dong, S., Livne, E., & Fernández, R. 2013, *ApJ*, 778, L37

Kushnir, D., & Katz, B. 2015, *ApJ*, 811, 97

Kushnir, D. 2019, *MNRAS*, 483, 425

Kushnir D., Waxman E., Chugunov A. I., 2019, *MNRAS*, 486, 449

Kushnir D., Katz B., 2020, *MNRAS*, 493, 5413

Kushnir D., Wygoda N., Sharon A., 2020, *MNRAS*, 499, 4725. doi:10.1093/mnras/staa3017

Livne, E. 1990, *ApJ*, 354, L53

Livne, E. 1993, *ApJ*, 412, 634

Maoz D., Mannucci F., Nelemans G., 2014, *ARA&A*, 52, 107

Moll R., Raskin C., Kasen D., Woosley S. E., 2014, *ApJ*, 785, 105

Moore, K., Townsley, D. M., & Bildsten, L. 2013, *ApJ*, 776, 97

Nomoto, K. 1982a, *ApJ*, 253, 798

Nomoto, K. 1982b, *ApJ*, 257, 780

Nugent, P., Baron, E., Branch, D., Fisher, A., & Hauschildt, P. H. 1997, *ApJ*, 485, 812

Paxton, B., Bildsten, L., Dotter, A., et al. 2011, *ApJS*, 192, 3

Paxton, B., Cantiello, M., Arras, P., et al. 2013, *ApJS*, 208, 4

Paxton, B., Marchant, P., Schwab, J., et al. 2015, *ApJS*, 220, 15

Perley D. A., Fremling C., Sollerman J., Miller A. A., Dahiwalé A. S., Sharma Y., Bellm E. C., et al., 2020, *ApJ*, 904, 35. doi:10.3847/1538-4357/abb98

Polin A., Nugent P., Kasen D., 2019, *ApJ*, 873, 84

Sharon A., Kushnir D., 2020a, *MNRAS*, 496, 4517. doi:10.1093/mnras/staa1745

Sharon A., Kushnir D., 2020b, *RNAAS*, 4, 158. doi:10.3847/2515-5172/abb9a3

Sharon A., Kushnir D., 2022, *MNRAS*, 509, 5275. doi:10.1093/mnras/stab3380

Shen, K. J., & Bildsten, L. 2014, *ApJ*, 785, 61

Shen, K. J., & Moore, K. 2014, *ApJ*, 797, 46

Shen K. J., Toonen S., Graur O., 2017, *ApJL*, 851, L50

Shen K. J., Kasen D., Miles B. J., Townsley D. M., 2018, *ApJ*, 854, 52

Sim S. A., et al., 2010, *ApJL*, 714, L52

Timmes, F. X., & Arnett, D. 1999, *ApJS*, 125, 277

Timmes, F. X., & Swesty, F. D. 2000, *ApJS*, 126, 501

Townsley D. M., Miles B. J., Shen K. J., Kasen D., 2019, *ApJL*, 878, L38

Vallely P. J., Tucker M. A., Shappee B. J., Brown J. S., Stanek K. Z., Kochanek C. S., 2020, *MNRAS*, 492, 3553

Woosley, S. E., & Weaver, T. A. 1994, *ApJ*, 423, 371

Woosley, S. E., & Kasen, D. 2011, *ApJ*, 734, 38

Wygoda, N., Elbaz, Y., & Katz, B. 2019, *MNRAS*, 484, 3941

Yakovlev, D. G., & Shalybkov, D. A. 1989, *Astrophysics and Space Physics Reviews*, 7, 311

Zel'dovich, Ya B. 1980, *CoFl*, 39, 211

Zingale M., Nonaka A., Almgren A. S., Bell J. B., Malone C. M., Orvedahl R. J., 2013, *ApJ*, 764, 97. doi:10.1088/0004-637X/764/1/97

which is available through the JINA reaclib data base⁵ (JINA, Cyburt et al. 2010). For the partition functions, $w_i(T)$, we used the fit of Kushnir (2019) for the values that are provided in the file WINVN_V2.0.DAT over some specified temperature grid. The forward reaction rates are taken from JINA (the default library of 2017 October 20). All strong reactions that connect between isotopes from the list are included. Inverse reaction rates were determined according to a detailed balance. Enhancement of the reaction rates due to screening corrections is described at the end of this section. We further normalized all the channels of the $^{12}\text{C}+^{16}\text{O}$ and $^{16}\text{O}+^{16}\text{O}$ reactions such that the total cross-sections are identical to the ones provided by Caughlan & Fowler (1988), while keeping the branching ratios provided by JINA. We ignore weak reactions and thermal neutrino emissions.

The EOS is composed of contributions from electron–positron plasma, radiation, ideal gas for the nuclei, ion–ion Coulomb corrections and nuclear level excitations. We use the EOS provided by MESA for the electron–positron plasma, for the ideal gas part of the nuclei, for the radiation and for the Coulomb corrections (but based on Chabrier & Potekhin (1998) and not on Yakovlev & Shalybkov (1989), see below). The electron–positron part is based on the *Helmholtz* EOS (Timmes & Swesty 2000), which is a table interpolation of the Helmholtz free energy as calculated by the Timmes EOS⁶ (Timmes & Arnett 1999) over a density–temperature grid with 20 points per decade. This is different from Kushnir (2019), where the Timmes EOS was used for the electron–positron plasma, since the *Helmholtz* EOS is more efficient and because the internal inconsistency of the *Helmholtz* EOS (see Kushnir 2019, for details) is small enough within the regions of the parameter space studied here. We further include the nuclear level excitation energy of the ions, by using the $w_i(T)$ from above.

We assume that the Coulomb correction to the chemical potential of each ion is given by $\mu_i^C = k_B T f(\Gamma_i)$ and is independent of the other ions (linear mixing rule (LMR), Hansen et al. 1977), where k_B is Boltzmann’s constant, $\Gamma_i = Z_i^{5/3} \Gamma_e$ is the ion coupling parameter, where Z_i is the proton number, and $\Gamma_e \approx (4\pi\rho N_A Y_e/3)^{1/3} e^2/k_B T$ is the electron coupling parameter, where N_A is Avogadro’s number and $Y_e \approx \sum_i X_i Z_i/A_i$ is the electron fraction. We use the three-parameter fit of Chabrier & Potekhin (1998) for $f(\Gamma)$. Following Khokhlov (1988), we approximate the LMR correction to the EOS by $f(\Gamma)$ for a ‘mean’ nucleus $\Gamma = \bar{Z}^{5/3} \Gamma_e$, where

$$\bar{Z} = \frac{\sum_i Y_i Z_i}{\sum_i Y_i}. \quad (\text{A1})$$

The screening factor for a thermonuclear reaction with reactants $i = 1, \dots, N$ and charges Z_i is determined from detailed balance (Kushnir, Waxman & Chugunov 2019):

$$\exp\left(\frac{\sum_{i=1}^N \mu_i^C - \mu_j^C}{k_B T}\right), \quad (\text{A2})$$

where isotope j has a charge $Z_j = \sum_{i=1}^N Z_i$ (same as equation (15) in Dewitt et al. 1973, for the case of $N = 2$).

This paper has been typeset from a $\text{\TeX}/\text{\LaTeX}$ file prepared by the author.

APPENDIX A: INPUT PHYSICS

Our input physics, which we briefly summarize below, are the ones used by Kushnir & Katz (2020). A detailed description can be found in (Kushnir 2019).

The nuclear masses are taken from the file WINVN_V2.0.DAT,

⁵ <http://jinaweb.org/reaclib/db/>

⁶ <http://cococubed.asu.edu/>